AGU Advances

RESEARCH ARTICLE
10.1029/2020AV000258

Wildfire Smoke Particulate Matter Concentration Measurements Using Radio Links From Cellular Communication Networks

Adrien Guyot[1], Jayaram Pudashine[1], Remko Uijlenhoet[2,3], Alain Protat[4], Valentijn R. N. Pauwels[1], Valentin Louf[4,5], and Jeffrey P. Walker[1]

[1]Department of Civil Engineering, Monash University, Melbourne, VIC, Australia, [2]Department of Water Management, Delft University of Technology, Delft, The Netherlands, [3]Hydrology and Quantitative Water Management Group, Wageningen University, Wageningen, The Netherlands, [4]Australian Bureau of Meteorology, Melbourne, VIC, Australia, [5]School of Earth, Atmosphere and the Environment, Monash University, Melbourne, VIC, Australia

Key Points:

- The 2019–2020 mega wildfires in Australia created hazardous health conditions due to smoke entrainment within the atmospheric boundary layer
- Low-level surface-based ducting conditions were identified for each of these smoke haze events in Greater Melbourne
- Radio links signal levels exhibited distinct patterns that can be used to retrieve surface smoke particulate matter concentrations

Supporting Information:

- Supporting Information S1
- Original Version of Manuscript
- Peer Review History
- First Revision of Manuscript [Accepted]
- Author Response to Peer Review Comments

Correspondence to:

A. Guyot,
adrien.guyot@monash.edu

Citation:

Guyot, A., Pudashine, J., Uijlenhoet, R., Protat, A., Pauwels, V. R. N., Louf, V., & Walker, J. P. (2021). Wildfire smoke particulate matter concentration measurements using radio links from cellular communication networks. *AGU Advances*, *2*, e2020AV000258. https://doi.org/10.1029/2020AV000258

Received 28 JUL 2020
Accepted 12 JAN 2021

Author Contributions:

Conceptualization: Adrien Guyot
Formal analysis: Adrien Guyot
Funding acquisition: Remko Uijlenhoet, Valentijn R. N. Pauwels, Jeffrey P. Walker

Abstract The monitoring of wildfire smoke is important to help mitigate impacts on people such as by sending early warnings to affected areas. Received signal levels (RSLs) from radio links have been used as an opportunistic way to accurately measure rainfall and humidity. Radio links provide integrated measurements along their paths and are an exceptional untapped resource to complement air quality stations in areas affected by smoke events, or in developing countries without air quality monitoring capability. This study analyzed radio link signal fluctuations during smoke events associated with the 2019–2020 Australian wildfires. Concurrently, the atmospheric boundary layer was characterized using atmospheric soundings and surface observations, as well as air quality proxies such as particulate matter concentrations less than 2.5 μm (10 μm), or $PM_{2.5}$ (PM_{10}). Observations showed that dry air containing large amounts of smoke within a surface layer above the ground acted as a lid, reducing dispersion, trapping and maintaining high ground-level concentrations of smoke. These conditions also created anomalous propagation conditions for radio links and operational weather radars. Power-law relations between signal fluctuations and PM_{10} and $PM_{2.5}$ were derived based on the link data collected and the closest air quality station observations. While there was variability in retrieval performance across smoke events, the best performance determination coefficients exceeded 0.5, with an RMSE on the order of less than 50 μg m^{-3} for concentrations of more than 400 μg m^{-3}. Mid-range link lengths (5–20 km) provided the best results.

Plain Language Summary Unprecedented mega wildfires in southern and eastern Australia generated considerable amounts of smoke and subsequent hazardous health conditions in Australian capital cities. We analyzed the atmospheric conditions during these smoke haze events within Greater Melbourne. Dry air containing large amounts of smoke sitting above the ground acted as a lid, reducing dispersion, trapping and maintaining high ground-level concentrations of smoke. Shallow planetary boundary layer at night also contributed to elevated concentrations. These conditions also created anomalous propagation conditions for radio links from cellular communication networks. Unique signal patterns were identified and shown to be related to these specific atmospheric conditions and smoke concentrations by analyzing the received signal levels of these links. It is proposed that these routinely recorded data by telecommunication companies be used to predict smoke concentrations at ground level during haze events.

1. Introduction

The impact of wildfire smoke on public health is becoming an issue of growing importance. In a warming climate producing more frequent and intense extreme weather conditions (IPCC, 2019; Jones et al., 2020; Reisinger et al., 2014), together with an increase of human population in fire-prone areas, extreme wildfires are more likely to occur, including fires producing large columns of convection such as for PyroCumulonimbus (Dowdy et al., 2018), ejecting large amounts of smoke into the troposphere and stratosphere (Kablick et al., 2020). In fact, in only the past few years, the occurrence of these extreme events have dramatically

Investigation: Adrien Guyot, Alain Protat, Valentijn R. N. Pauwels
Methodology: Adrien Guyot, Jayaram Pudashine, Remko Uijlenhoet, Alain Protat, Valentijn R. N. Pauwels, Valentin Louf, Jeffrey P. Walker
Project Administration: Remko Uijlenhoet, Jeffrey P. Walker
Supervision: Remko Uijlenhoet, Jeffrey P. Walker
Writing – original draft: Adrien Guyot
Writing – review & editing: Adrien Guyot

increased, for example, in Canada in 2015 (Fort McMurray; Wu et al., 2018), California in 2019, and Australia in 2019/2020 (Jones et al., 2020).

Flaming and smoldering combustion during wildfire events transform biomass and surrounding air into burning debris of various sizes, particulate matter (PM), and gaseous compounds. In the immediate proximity of the fire front and in the smoke plume, larger debris such as pyrometeors (McCarthy et al., 2020) are suspended aloft while the convection remains strong enough, with gravity eventually landing them on the ground within minutes to hours after emission. Conversely, PM and gaseous compounds disperse by various means, including cold and warm fronts, subsidence in valleys, and low-lying areas with little convection, and through entrainment in the atmospheric boundary layer (ABL). These smaller particles impact local, regional, or continental areas and remain in the atmosphere for extended periods of time (days, months, and years). Most concerning for human health impacts is the subsidence of these toxic gases and PM near ground level over large urban areas. While the nature and variability of the toxic PM and gaseous compounds are highly related to the type of biomass and combustion processes, of most concern for public health are the high concentrations of PM produced by wildfires (Reisen et al., 2015). Additionally, "aged" smoke PM is most likely to include higher amounts of organic content and presents an increased health risk (Keywood et al., 2015; Reisen et al. 2015). PM of less than 2.5 μm in diameter ($PM_{2.5}$) are the most impactful and affect all human organs and systems (Reisen et al., 2015), including deep penetration into the lungs that impair lung function (Xing et al., 2016). Borchers Arriagada et al. (2020) have shown that the high concentration levels of $PM_{2.5}$ associated with the 2019–2020 bushfires in eastern Australia were responsible for 417 deaths, 1,124 hospitalizations for cardiovascular problems, 2,027 respiratory problems, and 1,305 asthma-related issues. However, these authors limited their study to locations with available $PM_{2.5}$ observations, so the impact of smoke from these fires on population health is likely to have been understated.

Monitoring of air quality and specifically PM is routinely conducted by governmental agencies using dedicated stations and instrumental setup. $PM_{2.5}$ and PM_{10} (PM with diameter less than 10 μm) are often measured locally using filter-based samplers, light scattering methods, or beta attenuation monitors (Chung et al., 2001). Due to the prohibitive cost of maintaining air quality stations, local measurements of $PM_{2.5}$ and PM_{10} are scarce and often localized in densely populated urban areas in order to monitor emissions of $PM_{2.5}$ linked to road traffic. Spatially distributed observations of $PM_{2.5}$ have been derived from satellite observations, relying on measurements of aerosol optical depths and backscattering profiles (Gupta et al., 2007). The drawback of these observation techniques is a lower accuracy in the measurements as compared to ground-based stations. Measurements are often integrated over vertical profiles, not necessarily representative of concentrations of $PM_{2.5}$ close to the ground. The data coverage can sometimes be limited due to unfavorable weather conditions (Tian et al., 2010). Over the past 20 years, significant progress has been made to develop accurate smoke prediction models (Goodrick et al., 2013). A variety of models have been proposed (Kochanski et al., 2019; Y. Liu et al., 2019), with different degrees of complexity and more or less integration of detailed physical processes. Smoke modeling frameworks are operational tools that integrate the various components of the smoke modeling steps, including the fuel flaming and smoldering, the emissions, convective plumes, transport and dispersion, and eventually chemical transformation. An extensively used framework in the U.S. is BlueSky (Larkin et al., 2010) which has proven to provide reasonably accurate predictions although consistent underestimation of $PM_{2.5}$ concentrations when compared to satellite observations (Goodrick et al., 2013). Smoke prediction frameworks ingesting satellite observations of fire location and occurrence, such as High Resolution Rapid Refresh or HRRR (Ahmadov et al., 2017), provide real time maps of smoke and project smoke transport into the future. Ultimately, these frameworks tend to ingest a variety of data to improve the model predictions of smoke occurrence (Kim et al., 2020).

Radio links otherwise known as commercial microwave links (CMLs) are the backbone of cellular communication networks. The use of CMLs for opportunistic sensing of atmospheric variables was proposed almost two decades ago. One CML is made of a transmitting and a receiving antenna, operating in the microwave spectrum between 2 and 90 GHz and spanning over hundreds of meters to tens of kilometers. The most recent CMLs supporting the 5G networks (Fencl et al., 2020) operate at higher frequencies (71–76 and 81–86 GHz), while the older CMLs, which comprise most of the world's current point-to-point backhaul CMLs operate at lower frequencies (6–40 GHz).

Recorded attenuations of received signal levels (RSLs) due to scattering and absorption by raindrops has been shown to be directly due to the occurrence and intensity of rainfall; measuring rainfall intensity using the Beer-Lambert law of extinction was therefore made possible (Leijnse et al., 2007; Messer et al., 2006), taking into account factors such as wet antenna effects and the variability of the raindrop size distribution. In addition to rainfall, David et al. (2009, 2013) proposed to use CML signal fluctuations to detect and monitor the occurrence of fog or water vapor. Again, measured attenuation was shown to be linked to the concentration of air liquid water content and measured visibility.

The interaction of electromagnetic (EM) signals at microwave frequencies with burnt biomass-generated smoke has seen very few investigations (McCarthy et al., 2018). Most of the theoretical and observational work has been conducted at lidar wavelengths, in order to understand and model the scattering and absorption of light by smoke PM (L. Liu & Mishchenko, 2020). At microwave and radio frequencies, relatively long wavelengths (low frequencies) are much larger than the typical smoke aerosol diameter, and therefore do not interact directly with the suspended particles, in particular "aged" smoke transported further from the fire front. In order to produce significant and measurable scattering at microwave frequencies, fire-generated particles will have to be of the size of ash (in the order of mm), while aged smoke (micron-size particles) will have negligible scattering effect on the microwave EM signals. However, conditions of high smoke concentration could possibly produce or be linked to variations in the air refractivity. Anomalous propagation conditions have previously been identified in radio link RSLs and linked to pollution (David & Gao, 2016), sea-breeze (Rao et al., 1999) and synoptic weather patterns such as fronts (Arvola, 1957). To demonstrate the potential for monitoring smoke PM with such radio link RSLs fluctuations, data collected during conditions of smoke haze resulting from the large wildfires that occurred in South-East Australia during the Southern Hemisphere Summer period of 2019–2020 have been analyzed. In particular, data from over 100 radio links operating in the larger Metropolitan area of Melbourne were analyzed together with ABL vertical soundings and routinely measured air quality data including $PM_{2.5}$ and PM_{10}.

2. Material and Methods

2.1. Propagation of Electromagnetic Signals in the Atmospheric Boundary Layer

2.1.1. Refractive Index Fluctuations

The refractive index (n, dimensionless) describes the properties of EM wave propagation within a given volume. This index varies with wavelength and in the atmosphere, with n depending on the nature and properties of the air masses through which the EM wave is traveling. In particular, near the surface and within the ABL, n varies greatly as a function of local variations of air temperature, humidity, and pressure in the vertical and horizontal planes. These variations could be of diverse nature, either caused by stratification, larger-scale movement of air masses, mechanical or convective turbulence or the combination of all of these. In order to describe and resolve the propagation of an EM signal of a given wavelength within the ABL, the refractive index is typically decomposed as a sum of an average and its fluctuations. The scaling approach (Monin-Obukhov) can be used to describe the turbulence within the ABL using a defined set of parameters (Frehlich, 2000). The propagation of the EM waves can be described using the Helmholtz wave equation and solved using a split-step Fourier algorithm (Chou & Kiang, 2014). The aim of this paper is not to simulate EM propagation, but theoretical basics are presented here to guide the discussion on the results, which are extracted from case-study observations of radio link RSLs within the ABL.

2.1.2. Atmospheric Boundary Layer

The ABL vertical structure is commonly described using the potential temperature (θ, K), which can be estimated from the measured air temperature (T, K) and pressure (p, hPa) following:

$$\theta = T \times \left(\frac{p_0}{p} \right)^{2/7}, \tag{1}$$

with p_0 (hPa) the reference pressure (taken as 1,000 hPa). These variables are routinely measured in atmospheric soundings and can typically be used to characterize the static stability of an unsaturated atmosphere.

Stable, stratified conditions will see potential temperature increase with height ($\frac{\partial\theta}{\partial z} > 0$) while unstable conditions will see potential temperature decrease with height ($\frac{\partial\theta}{\partial z} < 0$).

2.1.3. Refractive Index Structure Parameter C_n^2

C_n^2 is a quantitative measure of optical scintillations, a phenomenon occurring when turbulent fluctuations in the refractive index of air can be observed, that is, variations in the speed at which the EM wavefront propagates (Tunick, 2003). The approach proposed by Tatarskii (1961) has been widely used for calculating the structure parameter of the refractive index of air C_n^2.

In this model, C_n^2 is related to the vertical gradient of refractivity assuming a stationary regime and a well-developed turbulence that follows the Kolmogorov law. Tatarskii (1971) derived a relation between the variance of the natural logarithm of the intensity of a signal ($\sigma^2_{\ln(I)}$) of a given wavelength λ (m) originating from a point source and C_n^2 according to:

$$C_n^2 = \frac{2^{14/3}\Gamma\left(\frac{7}{3}\right)\cos\left(\frac{\pi}{12}\right)}{\pi\sqrt{3\pi}\Gamma\left(\frac{8}{3}\right)} k^{-7/6} L^{-11/6} \sigma^2_{\ln(I)}, \tag{2}$$

with Γ the gamma function, k (m^{-1}) the wave number of the given signal ($2\pi/\lambda$), and L (m) the link length.

Later, Hill et al. (1980) proposed a relation between C_n^2 and the structure parameter of temperature (C_T^2, $K^2\ m^{-2/3}$) and moisture (C_Q^2, $kg^2\ m^{-2/3}$) such that:

$$C_n^2 = A_T^2 \frac{C_T^2}{T^2} + A_Q^2 \frac{C_Q^2}{Q^2} + 2A_T A_Q \frac{C_{TQ}}{TQ}. \tag{3}$$

The cross-structure parameter of temperature and humidity C_{TQ} can be written as $C_{TQ} = r_{TQ} C_T C_Q$, where r_{TQ} is the correlation coefficient between temperature and humidity (Kohsiek & Herben, 1983). The values of A_T and A_Q can be obtained from literature (Andreas, 1989).

At radio frequencies, fluctuations in moisture content due to turbulence play a dominant role in determining C_n^2 (that is, $C_Q^2 \gg C_T^2$) while temperature-related turbulence plays a more important role in near-visible wavelengths $\left(\text{that is } C_T^2 \gg C_Q^2\right)$. These properties led to the design of dedicated scintillometers for measuring either C_T^2 or C_Q^2, and by combining visible and microwave frequencies the cross-structure parameter C_{TQ} (de Bruin, 2002). In order to see large fluctuations in C_n^2 at radio frequencies, suitable conditions typically consist of high moisture content marine environments, or open water surfaces where latent heat fluxes are predominant (Leijnse et al., 2007). In contrast, continental surfaces dominated by sensible heat fluxes and characterized by lower air moisture content produce very little fluctuation in C_n^2 due to turbulence at radio frequencies.

2.1.4. Empirical Estimation of the Air Refractivity

The atmospheric refractive index can be computed (ITU-R P.453-14, 2019) using:

$$n = 1 + N \times 10^{-6}, \tag{4}$$

where N (dimensionless) is the refractivity that can be calculated following the approximate expression (ITU-R P.453-14, 2019):

$$N = 77.6\left(\frac{P}{T} + 4810\frac{e_p}{T}\right), \tag{5}$$

which has a reduced accuracy of 0.02% compared to the value obtained with the full expression for temperature ranges from −50°C to 40°C, with P the atmospheric pressure (hPa), T the absolute air temperature (K), and e_p the partial vapor pressure (hPa) calculated from:

$$e_p = \mathrm{RH} * e_s / 100, \tag{6}$$

with e_s the saturation vapor pressure (in Pa) calculated by:

$$e_s = 611\, e^{\left(\frac{17.27*T}{237.3+T}\right)}, \tag{7}$$

with T the air temperature (in °C). For a spherical earth, and a uniform refractive index across the atmosphere, EM rays are curved relative to the ground surface. The modified refractivity (M) enables approximation to a flat earth in which the refractive index varies with height z as z/R_e ($R_e = 6.371 \times 10^6$ the mean earth radius (m) and z (m) the height above the earth surface) calculated from N as:

$$M = N + 10^6 \times z / R_e. \tag{8}$$

2.1.5. Anomalous Propagation and Ducting

In engineering applications such as microwave propagation devices (weather radars, microwave links, antennae, etc.), vertical gradients of refractivity (dN/dz, with z the altitude in km) are typically used to define propagation conditions: subrefractive layers will see values greater than 0 km^{-1}, "normal" refraction will see values ranging from 0 to −78.7 km^{-1}, superrefractive conditions with values ranging from −78.7 km^{-1} to −157 km^{-1}, while the most extreme cases of superrefractive anomalous propagation conditions with values equal to or less than −157 km^{-1} create "ducting" conditions. These values are approximates deduced from EM propagation models using geometrical considerations on the earth curvature. There are three idealized types of ducts identified in the literature: surface ducts, surface-based ducts, and elevated ducts. Surface ducts are typically induced by temperature inversions; surface-based ducts are formed when elevated air is exceptionally warm and dry as compared to that of the surface. These types of ducts are known to occur between heights of 50 and 1,000 m above the ground surface. The refractive index fluctuations inside the ducts can be calculated using approaches combining a propagation model with a two-dimensional Kolmogorov spectrum solved with a split-step Fourier algorithm. This enables the effect of turbulence on refractive index fluctuations to be taken into account, in addition to the larger scale layering of the refractivity. Chou and Kiang (2014) used a split-step Fourier approach to simulate real case-study observations of vertical profiles of refractivity in order to evaluate the effect of turbulence on EM propagation in the occurrence of ducts and for different ABL conditions. They show that in the unstable case, the effect of turbulence is negligible, while in the stable case, the effect of mechanical turbulence induces energy leakage from ducting and non-ducting regions and leads to a more uniform distribution of signal attenuation within the duct.

2.2. Scaling Law Hypotheses for Particulate Concentration

2.2.1. The Unstable Case: Scintillation Due to Turbulence

Observed fluctuations of link RSLs $\sigma^2_{\ln(I)}$ are directly related to variations in the refractive index of air and its structure parameter C_n^2, which itself is related to fluctuations of C_Q^2 and C_{TQ} at frequencies of 5–40 GHz. At these frequencies, there is more sensitivity to water (i.e., as compared to temperature for near visible), so for fluctuations to be observed, conditions should likely be more humid rather than dry. If there are fluctuations in C_Q^2 and/or C_{TQ} due to heterogeneities in the turbulent eddies linked to moisture fluctuations or correlated temperature-moisture variations, these would be related to fluctuations in PM concentration.

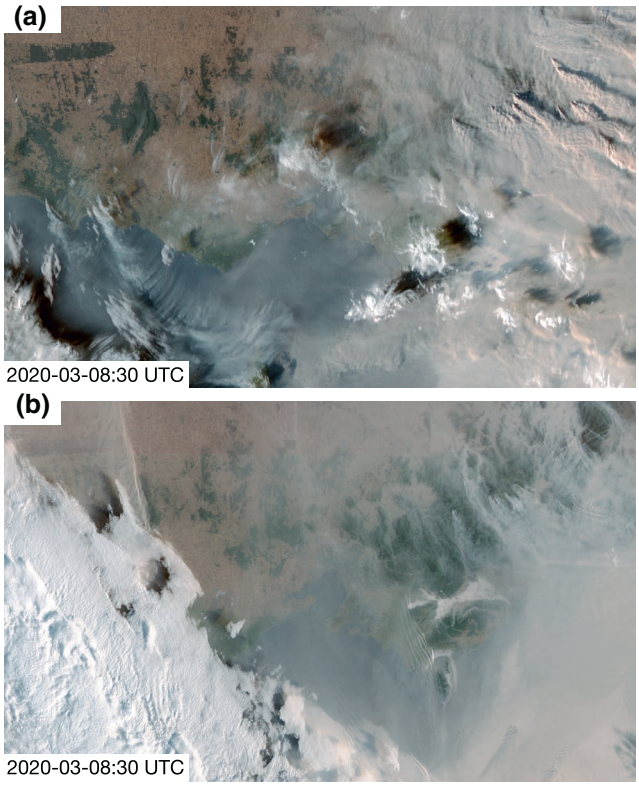

Figure 1. Satellite imagery (Himawari-8) true visible colors, showing Greater Melbourne in the center of each subpanel in: (a) late evening on the 3rd of January; (b) early morning on the 4th of January.

In fact, the PM concentration will follow a Poisson distribution, where the larger the PM concentration, the larger its variation across time and space, with these variations in concentration related to the strength of turbulent eddies and humidity and temperature heterogeneities.

2.2.2. The Stable Case: Anomalous Propagation

In the stable case, the layering of the refractive index induces anomalous propagation conditions, either surface ducting, surface-based ducts or elevated ducts, depending on the location of the temperature inversion (Fabry, 2015; Mentes & Kaymaz, 2007). The full-scale of processes in the ABL is complex, but as a simplification one can assume that a high smoke concentration will create stronger temperature inversions: the presence of a larger number of PM induces higher absorption in elevated air layers, and reduces further radiation reaching the ground, therefore increasing the strength of the inversion. This in turn would increase the contrast between layers of refractivity and produce a stronger gradient of dN/dz, producing strong ducting conditions. PM concentrations could thus be assumed to be linked to the strength of dN/dz, which itself would be expressed in larger variations in RSLs (large increases in RSL, or large decreases in RSL). However, in this case, the location of the duct or superrefractivity layer combined with the geometry of the links (elevation of receiver and transmitter antennas, and effective height above ground) will have an important effect as well.

For both the unstable (scintillation) and stable (anomalous propagation) cases, it is hypothesized here that the variations in RSLs ($\sigma^2_{\ln(I)}$) are linked to PM concentrations (PM_{10} and $PM_{2.5}$) via a power relation of the type $PM = a\ \sigma^2_{ln(I)}{}^{b}$, where the a and b parameters can be determined by the best fit based on the observations. This is based on similarities with other proxies such as temperature or humidity; in terms of fluctuations the case of scintillation, or vertical gradients of temperature or humidity for the stable case.

2.3. Study Area and Context

The severity and unprecedented scale of the 2019–2020 mega wildfires in eastern and southern Australia, also known as "Black Summer," generated considerable destruction of biomes and natural habitats, with a total burnt area of more than 18.6 M ha, 34 fatalities, and more than 5,900 properties and buildings destroyed (Boer et al., 2020). The large amounts of burnt biomass produced considerable emissions of smoke and PMs, which dispersed locally, regionally, and globally. Some of these megafires burnt for as long as 19 weeks (Boer et al., 2020). The mesoscale weather conditions created varying dispersion mechanisms for the emitted smoke, sometimes entrapping high concentrations of smoke in valleys or low-lying areas, while other more suitable conditions enabled efficient dispersion.

The eastern and southern Australian capital cities (Canberra, Sydney, Melbourne, and Brisbane) suffered long-lasting and high concentration exposure to $PM_{2.5}$, especially Sydney and Canberra, where these conditions lasted for several weeks. Because of the influence of south-westerlies, Melbourne was less exposed but experienced a series of major smoke events lasting in the order of 12–48 h for each event during January 2020. Accordingly, this study focused on the area of Greater Melbourne, where access to CML data has been made possible through another experiment focusing on rainfall measurements (Pudashine et al., 2020).

Figure 1 shows in true visible colors an area comprising Greater Melbourne (at the center of each subpanel) and the Australian Alps to the East, where smoke plume columns can be seen in subpanel (a). During January 2020, large fires burnt in the densely forested areas of the Australian Alps (Northern and Gippsland areas), with fire fronts located at distances ranging from 150 to 400 km from Melbourne CBD. Generally,

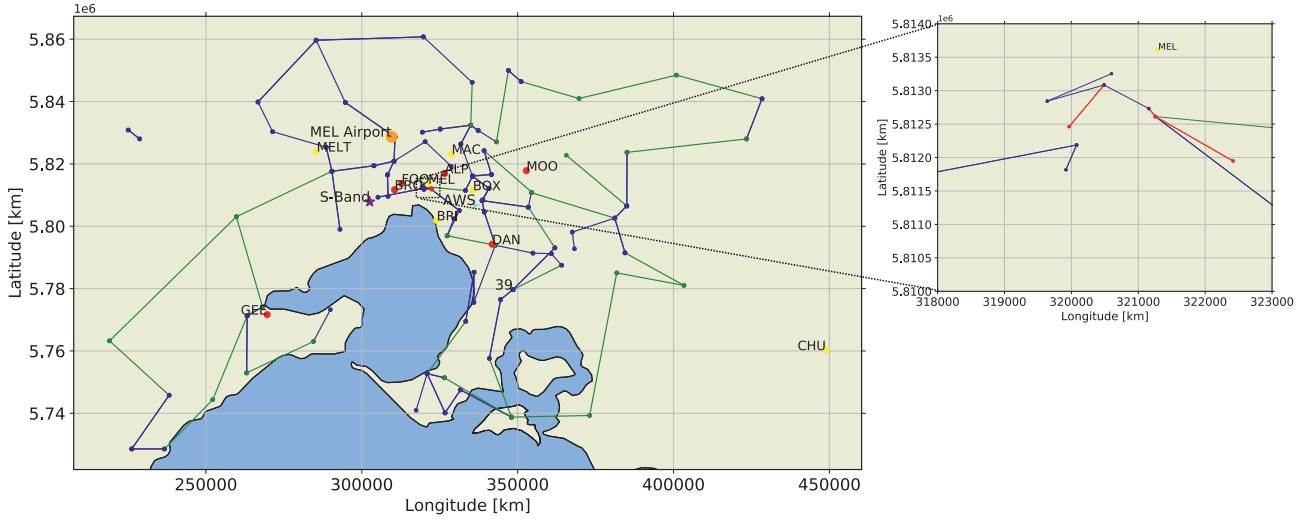

Figure 2. Location of the links (lines: green, $f < 10$ GHz; blue, 10 GHz $< f <$ 30 GHz; red, $f > 30$ GHz), air quality stations (red dots: measuring both $PM_{2.5}$ and PM_{10}; yellow dots, measuring $PM_{2.5}$ only), Melbourne airport (orange), S-Band weather radar (purple), automatic weather station (AWS) in Greater Melbourne.

intense fire activity is associated with high ground-level air temperature, low relative humidity, and strong wind, which are common during that time of the year. The mesoscale setup for the 3rd and 4th of January was typical for the events presented herein, with strong northerly or north-westerly winds pushing the fire smoke plumes to the southeast (Figure 1a), often breaking out of the ABL in the early morning when fire-generated convection is sufficient, and entraining a large amount of smoke in the free troposphere. The direction of the flow generally changed to northerly, or north-easterly toward the end of the day, pushing the smoke previously entrained in the free troposphere toward Melbourne. Subsidence and downdrafts ("wisps," Deardorff et al., 1969) gradually helped to increase the smoke concentration within the ABL (Pahlow et al., 2005). Concurrently, some of the smoke remained within the ABL and was further transported within the ABL at hundreds of km from its origin. In the case of the 4th of January, a south-westerly front (Figure 1b) including precipitation cleared the region from smoke, marking the end of that event.

2.4. CML and Weather Radar Data

RSL data from one of the cellular communication operators are available for this study within a radius of 200 km around the city of Melbourne. The total number of links was 178, including 64 duplex links and 50 single links, but 34 out of the 178 links did not operate over the study period, leaving 144 available links for analysis (Figure 2). The path lengths (L, m) ranged from 100 m to 30 km with the corresponding frequencies spanning from 6 to 39 GHz. The RSLs were sampled at 10 Hz with a resolution of 0.1 dB and the received signal power average (P_{avg}, dB), minimum (P_{min}, dB), and maximum (P_{max}, dB) stored at the end of each 15 min interval. All the links were vertically polarized except 9, which were horizontally polarized. The transmitted powers for all links remained constant. The full day of the 31st of January 2020 (AEDT) is the only gap in the data set, where data are unavailable for all the links.

An S-Band weather radar operated by the Australian Bureau of Meteorology (BoM) collected data over the study area and was located at Laverton (37°51'36" S, 144°45'36"E) being 44 m above sea level (Figure 2). From the radar ground clutter reflectivity data, maps of the 95th percentile of ground clutter reflectivity (Z_{95}, dB) were produced at 6-min resolution using the relative calibration adjustment approach proposed by Louf et al. (2019) within a 10 km range around the radar. Ground clutter pixels were identified by a frequency of occurrence above 95%, a reflectivity above 50 dBZ and a cross-correlation coefficient <0.5. In normal conditions, the monitoring of Z_{95} allows a quality check of the radar calibration constant. Here, the idea was to use the observed changes in Z_{95} to monitor conditions of superrefractivity or ducting: in these conditions, the radar beam would bend further to the ground, leading to an increase of Z_{95}. Differences in Z_{95} of as little as 0.2 dB can be confidently detected with this technique.

2.5. Ground Weather and Atmospheric Profile Sounding Data

A Vaisala WXT520 automatic weather station dedicated to the study of rainfall using radio links (Pudashine et al., 2020) was installed at Mt Waverley Reservoir (Figure 2) to measure air temperature (T, °C) and humidity (RH, %). These observations were used as reference for the variable time-series presented in this study.

Rain gauges operated by the BoM and the local water agency (Melbourne Water) were used to detect periods of rainfall for each link following the same procedure as described in Pudashine et al. (2020). A total of 168 gauges operated by Melbourne Water and 258 gauges operated by the BoM with a tipping resolution of 0.2 mm and temporal resolution of 6 min were used.

Atmospheric soundings were conducted at Melbourne airport (Figure 1) twice per day, at 00 UTC (9 a.m. AEDT) and 12 UTC (9 p.m. AEDT), except for some days where soundings were not available. Soundings were automatically retrieved from a web-based archive (http://slash.dotat.org/cgi-bin/atmos). For each sounding, atmospheric pressure (P, hPa), air temperature (T, °C), dew point (T_d, °C), wind direction and speed (u, m s^{-1}) and altitude (z, m) were measured at regular intervals to build a vertical profile of atmospheric variables. From these, the refractivity N and the gradient of refractivity (dN/dz) were derived using Equation 4, and the modified refractivity using Equation 8, respectively. For each 12 UTC sounding, data for the first two altitudes (the closest to the ground) were erroneous, either filled with zeros, or spurious data. These were removed from further analysis. Ground observations from an automated weather station operated by the BoM (station 86282) were used to fill observation gaps at ground level, and additional values of refractivity and dN/dz were calculated for the intermediate datapoints using a linear interpolation between ground-level values and values for the 3rd level observation of each 12 UTC sounding.

2.6. Air Quality Data

The environmental protection agency (EPA) of the Australian state of Victoria operates a number of air quality stations across the Melbourne metropolitan areas, which were used in this study as a reference comparison against the RSLs from the radio links. There were 7 stations within Greater Melbourne measuring both PM_{10} and $PM_{2.5}$ and 6 stations measuring only $PM_{2.5}$ (Figure 2, Table S1). A tapered element oscillating microbalance monitor continually measured the concentration of PM_{10}. Two methods were used to monitor $PM_{2.5}$: (i) standard beta attenuation monitors automatically measured and recorded airborne particles by collecting these on a filter tape and measuring the reduction in beta rays traveling through the particles; (ii) light-scattering sensors automatically measured the number of particles passing through a beam, using light scattering and attenuation to record the concentration of particles in the air. In addition to PM_{10} and $PM_{2.5}$, the EPA also deployed instruments to measure the visibility and carbon monoxide (CO) at selected locations. Carbon monoxide concentrations (CO, ppm) were measured using an infrared closed-path instrument. Visibility (Vis, 1/mm) was measured based on light scattering using a nephelometer. Only two sites (Geelong South and Alphington) displayed simultaneous records of PM_{10}, $PM_{2.5}$, CO and Visibility. For each of these two sites, CO and Visibility were compared to PM_{10}, $PM_{2.5}$. All measurements were averaged to 1-hour intervals.

3. Results

3.1. Received Signal Levels and Z_{95} during Smoke Events

RSLs of one reference link (frequency of 15.2 GHz and length of 19 km) were used to illustrate typical signal patterns for the full period of interest ranging from early January to early February 2020. Figure 3 shows the time-series of the link RSL together with the radar Z_{95} as well as environmental variables as measured by the different sensors. Thresholds of 27 μg m^{-3} for $PM_{2.5}$ and 50 μg m^{-3} PM_{10} were used to define smoke pollution events under Australian regulations and are used hereafter to define "smoke events," when one of these criteria is met. At the two sites where comparisons were possible, very strong correlations were found between visibility and $PM_{2.5}$ (and PM_{10}) with correlation coefficients of 0.97 and 0.98 for PM_{10} and around 0.9 for $PM_{2.5}$ (Figures S1 and S2). High correlation coefficients were also found when comparing $PM_{2.5}$ (and PM_{10}) to CO. This supported the use of only PM_{10} and $PM_{2.5}$ to compare to RSLs in this study. Six events have

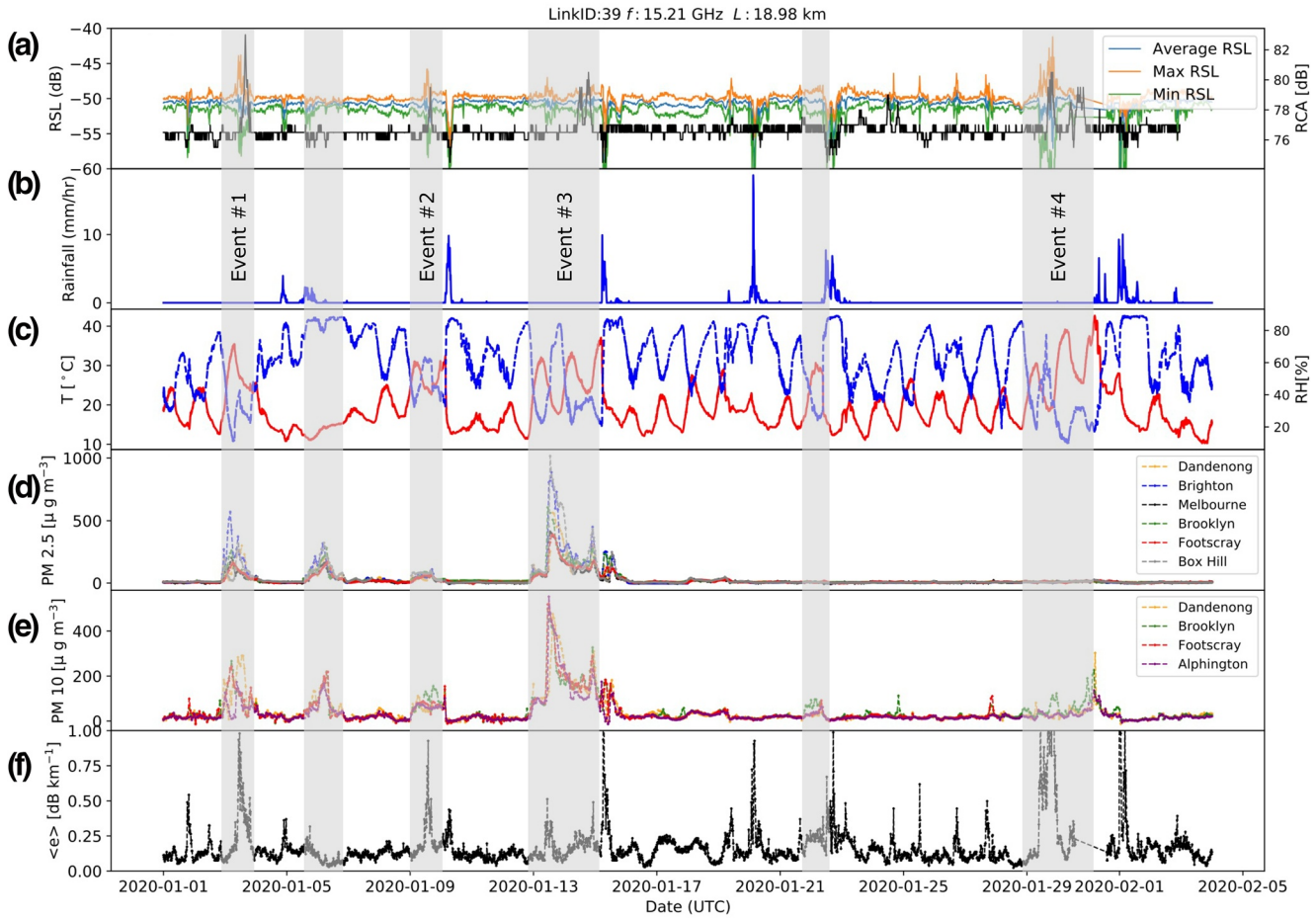

Figure 3. Time-series for January and early February 2020 of: (a) RSL for link #39 and S-Band Z_{95}; (b) rainfall; (c) ground-level air temperature and humidity; (d) $PM_{2.5}$; (e) PM_{10}; and (f) entropy $<e>$.

been identified based on the time-series of $PM_{2.5}$ and PM_{10} (Figures 3d and 3e). Two of these events coincide with rain events and are not considered for further analysis due to the complexity of interpreting mixed signatures when rainfall is present. Four events are retained and labeled for the analysis (E#1 for event #1, and so on), with the end of some of the events being marked by the occurrence of rainfall (for E#1, E#3, and E#4). Each of these four events was associated with elevated air temperatures and low relative humidity. Indeed, such conditions are typically necessary for triggering an increased wildfire activity and subsequent generation of smoke on fire grounds hundreds of km away to the east of the city.

During rainy events, RSLs typically followed the behavior described in the literature (Leijnse et al., 2007), where the average (as well as the minimum and maximum) RSLs decreased proportionally with the rainfall rate. Outside of the rainy events, the RSL fluctuated but the average remained roughly equal to its baseline (previous 24 h-centered window). Remarkably, during the smoke events, the values of the maximum and minimum RSL over 15 min intervals reached further extreme values (larger maximum and lower minimum). Since the RSL was sampled at 10 Hz, the maximum and minimum are the outer shape of a distribution of values (possibly a normal distribution), or the outliers of that distribution. Coincidentally, during smoke events, Z_{95} peaked at values of a couple dB to up to 5 dB above the baseline Z_{95}, which itself remained constant at around 77 dB. In Figure 3f, the difference between the 15-min maximum and minimum, normalized by the link path length is shown and labeled as $<e>$ (dB km^{-1}) for "entropy." The rationale for using the difference between the maximum and minimum for comparison with PM_{10} and $PM_{2.5}$, versus only the minimum or maximum, is discussed in the next section.

3.2. Relations Between Received Signal Levels and $PM_{2.5}$ and PM_{10}

In order to investigate which of P_{max}, P_{min} or a combination of P_{max} and Pmin is the best proxy to compare to PM as measured locally, linear regressions were performed for $(P_{max}-P_{min})/L$, P_{min}/L, and P_{max}/L against $PM_{2.5}$ and PM_{10}. The received power values were divided by the corresponding link path length to normalize the received values (in dB km^{-1}) in order to facilitate comparison between RSLs from various links. To find the closest PM station, the minimum distance between the centerpoint of the link and the station location was found. Figure S3 shows the distribution of the coefficient of determination values for each regression type, type of PM, and for each of the four events. There is variability among events, with E#1 and E#2 performing considerably better than E#3 and E#4. The possible reasons behind these disparities are discussed in the next section, where events are analyzed individually. For both $PM_{2.5}$ and PM_{10} and for all events, the signal most relevant to compare with PM concentrations appears to be P_{max}, with P_{min} performing considerably worse. However, the combination of P_{max} and P_{min}, in terms of their difference (in dB, normalized by the path length), led to a smaller spread in R^2 than seen when using P_{max} only, while keeping the same average performance (mean of R^2 for each of the regression subsets). In addition, using $(P_{max}-P_{min})/L$ enabled to provide a standard value (dB km^{-1}) independent from each RSL baseline value, and made comparison of regression coefficients across different links possible.

3.3. Event-Based Analysis

Each of the four events of January 2020 were analyzed separately, using time-series of the entropy for selected links grouped into frequency ranges ($f < 10$ GHz, 10 GHz $< f <$ 30 GHz), together with concentrations as measured by the PM stations, as well as the S-Band radar Z_{95}. In addition, atmospheric profiles of modified refractivity (M, unitless) and of the gradient of refractivity with height (dN/dz, km^{-1}) are shown in side panels. These are plotted in Figures 4 and 5 and Figures S4 and S5.

3.3.1. Event #1: 3rd of January 2020

During the first event on 3rd of January 2020, particulate concentrations reached over 200 μg m^{-3} for PM_{10} and 500 μg m^{-3} for $PM_{2.5}$ at their peaks (Figure 4), being levels considered as hazardous for human health. Concentrations peaked at various times of the day for each PM measuring station, from the late afternoon in the western suburbs to the middle of the night for the eastern suburbs (Dandenong). The air temperature at ground level was around the climatic average for that time of the year, but the relative humidity was low (down to below 20% and remained relatively low at 30%–40% during the night-time). The radar Z_{95} showed a clear signature with an increase of up to 6 dB as compared to its baseline, with a maximum at 15:00 UTC. Lower frequency links (both categories < 30 GHz, on panels d and e) showed simultaneous increases in $<e>$ for some links (link 11 and 114), while for most of the selected links the $<e>$ values peaked at different times of the day, and often with a much wider peak base as compared to the radar Z_{95}. The $<e>$ values of high-frequency links (panel f) showed apparently random and little variation during that event. Vertical profiles of the modified refractivity showed the occurrence of a surface-based duct on the 3rd of January at 12:00 UTC, which is neither present on the morning sounding of the same day or on both soundings from the following day. This duct had a base located lower than 200 m above the ground at 12:00 UTC, although its spatial extent and homogeneity remained unknown. The potential temperature shows the presence of a stable layer from 100 to 400 m above ground level. The surface layer (below 100 m AGL) shows subrefractive conditions.

3.3.2. Event #2: 9th of January 2020

During the late morning of the 9th January 2020 (starting at 9:00 UTC), $PM_{2.5}$ and PM_{10} gradually increased to reach peak values during the late night (15:00 UTC), with varying concentrations of 50–100 μg m^{-3} for both PMs (Figure S4). The temperature was similar to E#1 but the relative humidity was significantly higher during the night (around 60%) as compared to E#1. The radar Z_{95} showed a distinct signature with an increase of 3 dB as compared to its baseline, with a similar peak shape as for E#1. Lower frequency links (both categories < 30 GHz, on panels d and e) showed simultaneous increases in $<e>$ for some links (links 11 and 114), while for the remainder of the selected links, their $<e>$ values peaked at different times of the night, and often with varying peak base widths as compared to the radar Z_{95}. The $<e>$ values of high-frequency links (panel f) showed little variation during that event, possibly due to random noise. Vertical profiles of

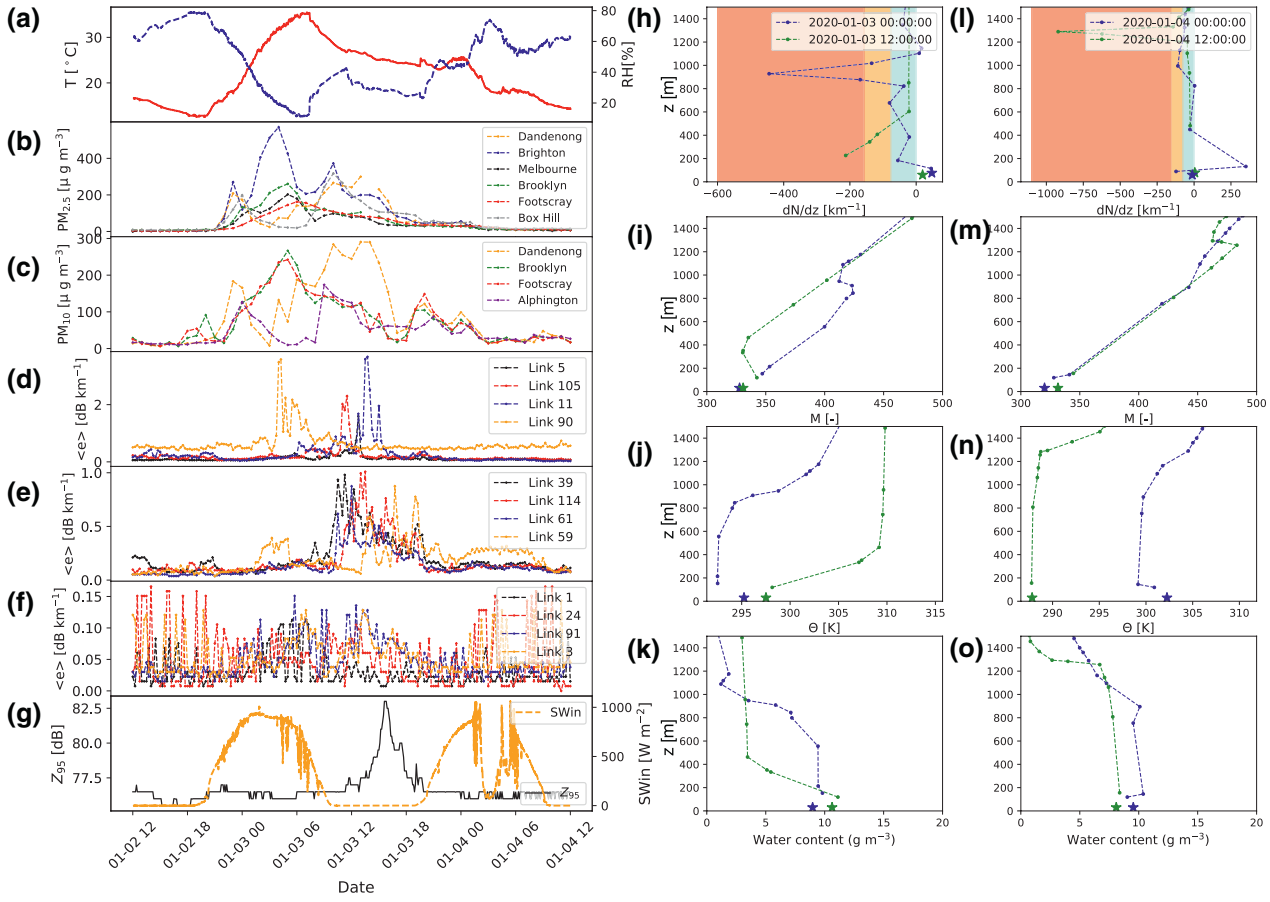

Figure 4. Time-series of selected variables for E#1: (a) Ground-level air temperature and relative humidity; (b) and (c) measured concentrations of $PM_{2.5}$ and PM_{10}, respectively; (d) entropy <*e*> for links with frequencies < 10 GHz; (e) entropy <*e*> for links with frequencies > 10 GHz and <30 GHz; (f) entropy <*e*> for links with frequencies > 30 GHz; (g) Z_{95} and incoming shortwave radiation *SWin*. The right panels show (h) and (l) the gradient of refractivity (*dN/dz*) as a function of altitude, (i) and (m) modified refractivity *M*, (j) and (n) potential temperature θ and, (k) and (o) water content, as derived from the soundings. Red shadings show the conditions for ducting, orange shadings for superrefraction, and cyan for normal conditions, while white show the subrefraction conditions. The first datapoint is shown as an asterisk since it is calculated using ground and sounding data and possibly more prone to uncertainties.

the modified refractivity showed the occurrence of a surface-based duct on the 9th of January at 12:00 UTC, which is neither present on the morning sounding of the same day or on both soundings from the following day. This duct had a base located at around 200 m above ground at 12:00 UTC, being therefore slightly higher than for the first event. The potential temperature shows the presence of a stable layer from 100 to 600 m above ground level, a larger depth than for the first event. Similarly, as for E#1, the near-surface layer (below 100 m AGL) showed subrefractive conditions.

3.3.3. Event #3: 13th and 14th of January 2020

This event spanned over a longer period, starting with a sharp increase in PM concentrations during the early night of the 13th January 2020 (9:00 UTC), shortly after sunset (Figure 5). $PM_{2.5}$ and PM_{10} quickly reached values of up to 1,000 and 500 μg m^{-3} respectively, with spatial variability in the timing of the maxima, with the south-western suburbs (Dandenong) showing delayed maxima. The concentration levels decreased steadily during the following day and night but remained at hazardous levels (above 200 μg m^{-3}) until reaching lower values during the day of the 15th January. The radar Z_{95} showed no variations during the night of the 13th January, and a double peak with increases of up to 3 dB from the Z_{95} baseline on the night of the 14th January, with peak widths covering the entire night-time. Ground-level relative humidity was high (above 80%) during the first night, and low (around 30%) during the second night, while the air temperature was similar as for the first two events. Lower frequency links (panels d and e) showed small variations in <*e*> during the first night (maximum values below 0.5 dB km^{-1}), although some of the

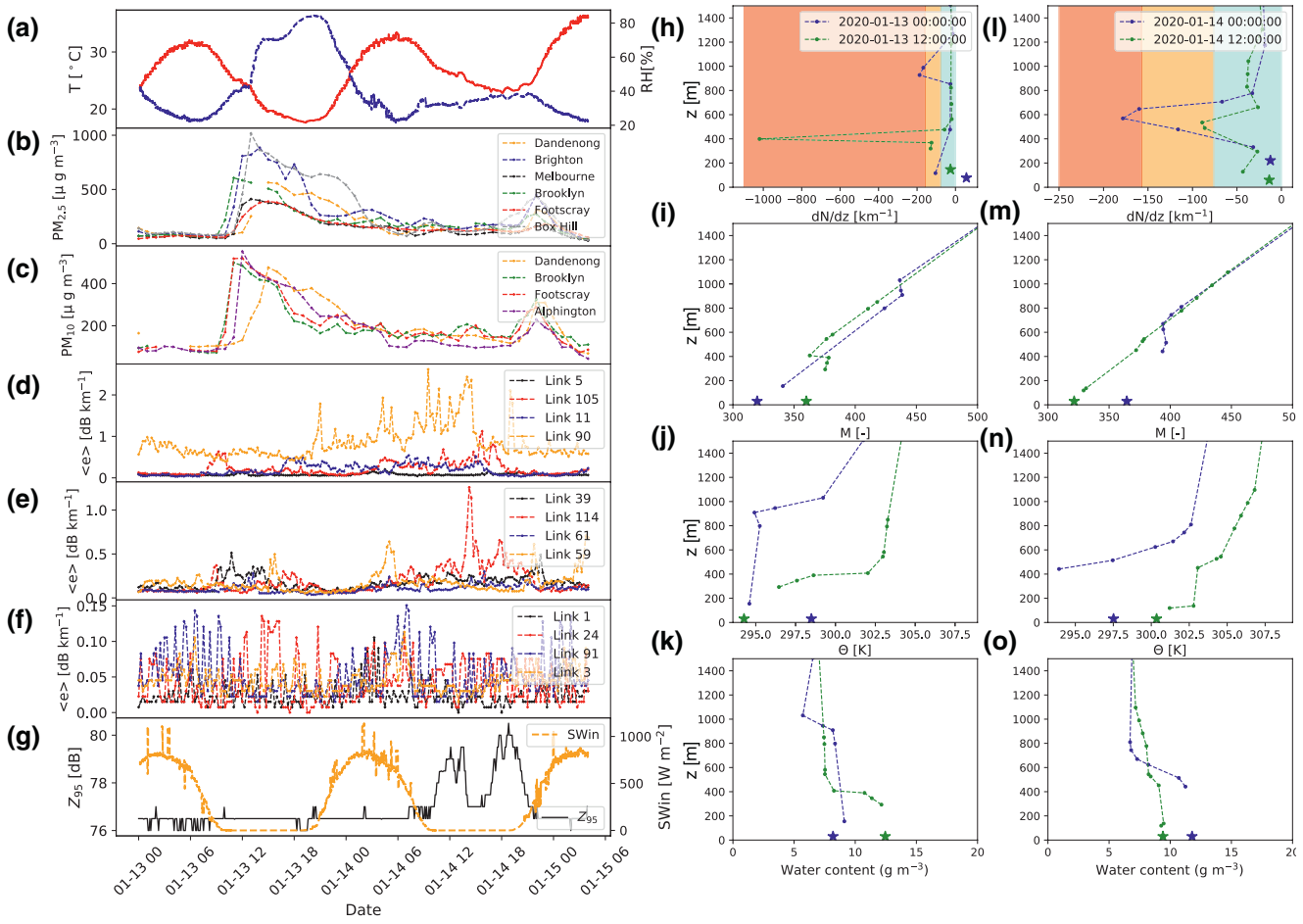

Figure 5. Time-series of selected variables for E#3: (a) Ground-level air temperature and relative humidity; (b) and (c) measured concentrations of $PM_{2.5}$ and PM_{10}, respectively; (d) entropy $<e>$ for links with frequencies < 10 GHz; (e) entropy $<e>$ for links with frequencies > 10 GHz and < 30 GHz; (f) entropy $<e>$ for links with frequencies > 30 GHz; (g) Z_{95} and incoming shortwave radiation *SWin*. The right panels show (h) and (l) the gradient of refractivity (dN/dz) as a function of altitude, (i) and (m) modified refractivity M, (j) and (n) potential temperature θ and, (k) and (o) water content, as derived from the soundings. Red shadings show the conditions for ducting, orange shadings for superrefraction, and cyan for normal conditions, while white show the subrefraction conditions. The first datapoint is shown as an asterisk since it is calculated using ground and sounding data and possibly more prone to uncertainties.

selected links showed no variations (link 5). Variations for the lower frequencies were again of the same order for the second night, although some links (e.g., 114) showed maxima of $<e>$ above 1 dB km^{-1}. Link 90 on the other hand showed significant variations during the entire period with maximum values above 2 dB km^{-1}. As for the first two events, the higher frequencies (panel f) showed only apparently random variations during that period.

Vertical profiles of the modified refractivity showed the occurrence of a surface-based duct on the 13th of January 2020 at 12:00 UTC, which was still present in both the morning and evening soundings of the 14th January. This surface-based duct had a base around 350 m and a shallow depth of 100–200 m at 12:00 UTC, deepening on the 14th January at 00:00 UTC to the 700 m AGL, while being slightly more shallow on the 14th January at 12:00 UTC and less pronounced (as seen in lower values of dN/dz). As for the first two events, the near-surface layer showed subrefractivity conditions, but in the case of this event, this near-surface layer seemed deeper (from ground level to 200 m, or even 300 m in the first night). Ground level relative humidity was high (above 75%) during the first night, and much lower on average during the second night (around 30%).

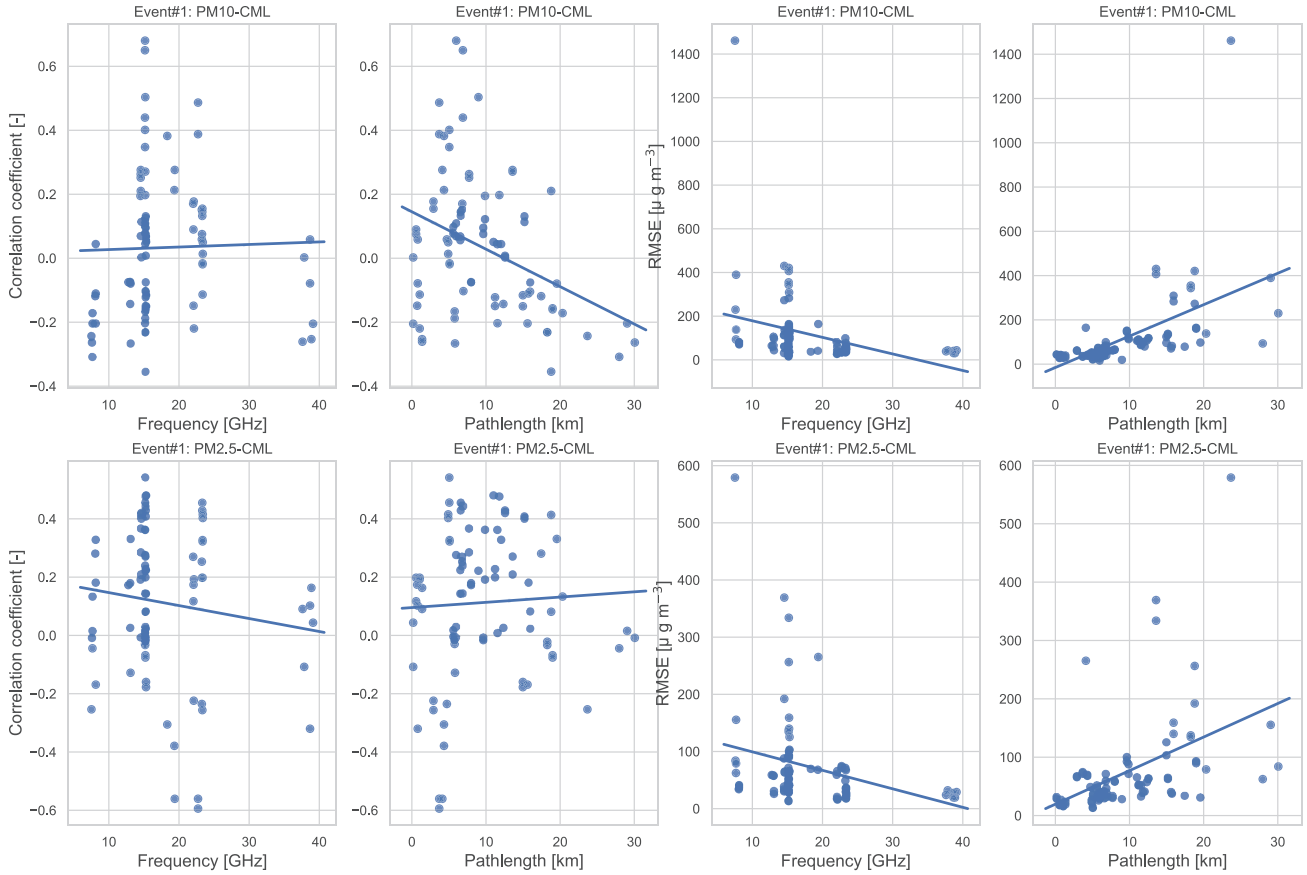

Figure 6. RMSE and correlation coefficients of the power-relations derived from link entropy and PM concentrations, versus link length and link frequency for E#1.

3.3.4. Event #4: 29th of January 2020

During this event, $PM_{2.5}$ remained relatively low (below 25 µg m^{-3}) but PM_{10} showed spatial variability with values above 100 µg m^{-3} in the western suburbs) (Figure S5). The ground level air temperature showed similar trends and values as the other events, while the humidity saw abrupt variations during the night of the 29th January, typical signatures of horizontal and vertical variability and mixing of air masses of different properties. A distinct peak in Z_{95} with a maximum of 4 dB increase as compared to its baseline and peak width of 4–5 h was observed. Simultaneous increases in <*e*> for lower frequency links were observed (panel d and e) with values above 2 dB km^{-1}. The timing of the maxima for these links was spread across the night with links 39 and 114 showing good synchronization with the Z_{95}, while the other links (105, 11) peaked much earlier in the night, suggesting strong spatial variability of PM over Melbourne. The sounding on the 29th January at 12:00 UTC displayed a temperature inversion (base around 100 m AGL), with a corresponding surface-based duct as shown in *dN/dz* and *M*. This duct was not apparent in the sounding on the 30th January at 00:00 UTC, but again a strong surface-based duct was evident in the 12:00 UTC sounding of the same day, with a low base at around 100 m AGL or less. During that second night, a clear signature in the Z_{95} was again observed but unfortunately CML data were not recorded for that day.

3.4. Effect of Link Length and Frequency on PM <*e*> Regressions

Power law regressions between PM concentration of nearby stations and entropy as measured by the links were performed, and the corresponding correlation coefficients and RMSE plotted in Figure 6 in order to investigate the effect of link length and frequency for the first event. For both $PM_{2.5}$ and PM_{10}, lower frequencies led to higher correlation coefficients and lower RMSE, while higher frequencies show lower correlation coefficients and higher RMSE. Middle-range pathlengths (5–20 km) provided higher correlation

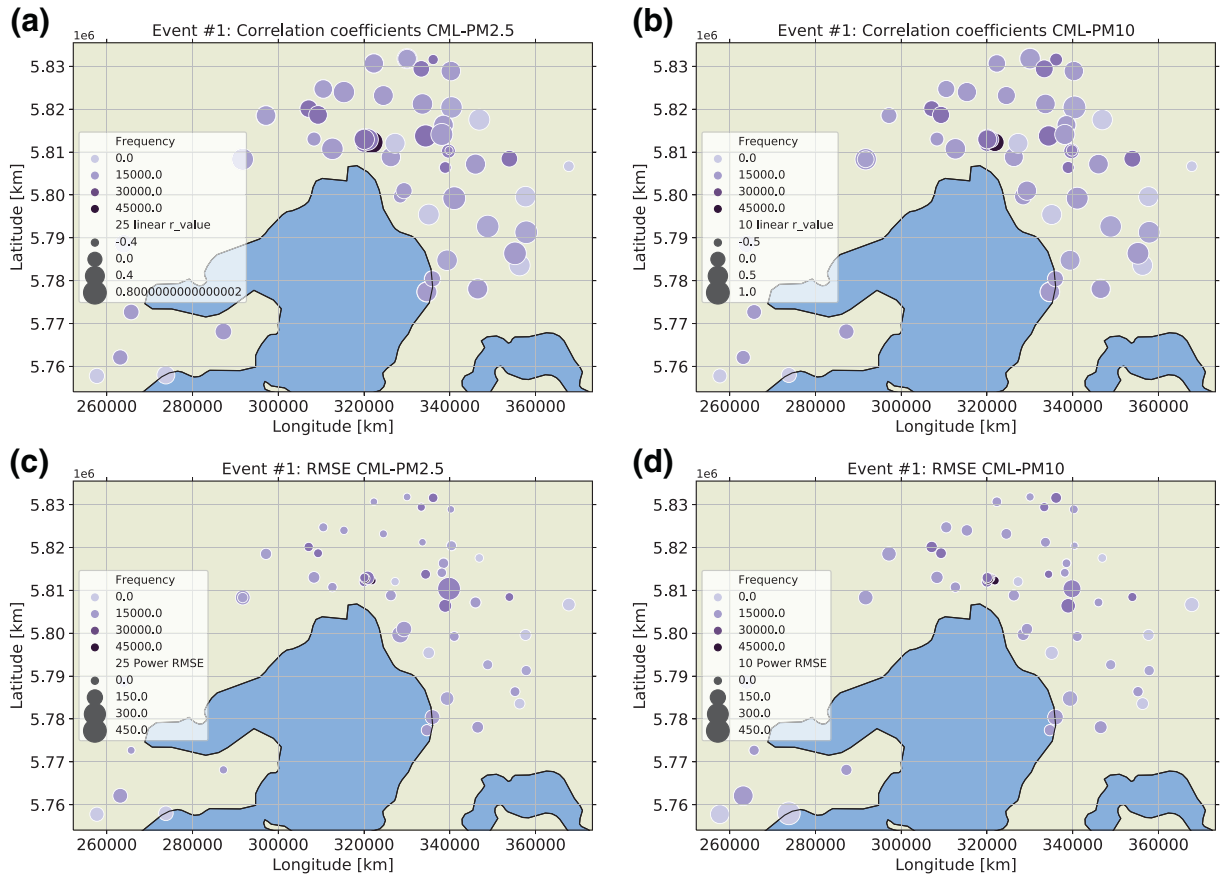

Figure 7. For Event #1, spatial distribution of correlation coefficients and RMSE of the linear regressions between CML-derived PM and local in-situ measured PM: (a) correlation coefficients for PM2.5; (b) correlation coefficient for PM10; (c) RMSE for PM2.5; (d) RMSE for PM10.

coefficients and lower RMSE. However, there could be a bias in this result because of the smaller number of short (<5 km) and very long (>20 km) paths links in these data sets. The geometry of the links, for example, the elevation of the transmitter and receiver antennas above ground and the effective height of the Fresnel zone above ground are likely to be important parameters, but this information was not readily available for this data set.

3.5. Spatial Extend of Smoke Events and Concentration Retrieval

In order to explore the spatial variability in the concentration retrievals using power-law relations between PM concentrations and link entropies, correlation coefficients and RMSE are shown over the study area, both for E#1 (Figure 7) and E#3 (Figure 8). For E#1, the correlation coefficients were relatively homogenous (~0.5) over the area for both $PM_{2.5}$ and PM_{10}, with the exception of the south-west (Geelong), where the values were the lowest, and for some individual links. The RMSE for E#1 followed the same spatial distribution, with higher values in the south-west and only for a few links. For E#3, high correlation coefficients and low RMSE values were restricted to the east of the domain, whereas in the other areas, most links showed lower correlation coefficients and higher RMSE values.

Values of the coefficients a and b of the $PM = a <e>^b$ regressions are shown in Figure 9. Apart from a few outliers, the coefficients a were within the range of 100–600, while b was in the range of 0.5–1.25 for PM_{10}. For $PM_{2.5}$, the coefficients were slightly more dispersed with a ranging from 100 to 800 and b from 0.55 to 1.50. No obvious dependency on the frequency was observed.

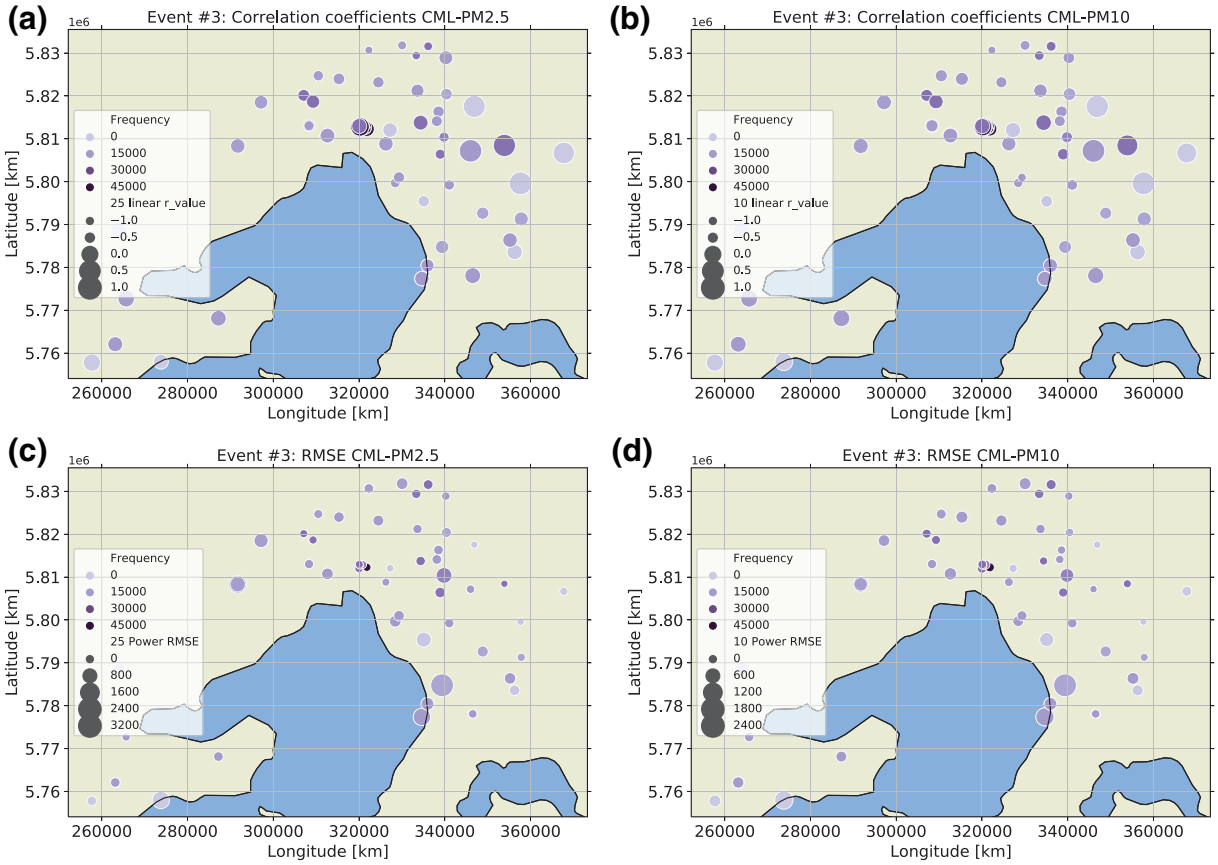

Figure 8. For Event #3, spatial distribution of correlation coefficients and RMSE of the linear regressions between CML-derived PM and local in-situ measured PM: (a) correlation coefficients for PM2.5; (b) correlation coefficients for PM10; (c) RMSE for PM2.5; (d) RMSE for PM10.

4. Discussion

4.1. Ducting and Scintillation

In this study, link RSLs were sampled at 1 Hz and stored at 15 min intervals: the difference between minimum and maximum normalized by the link path length, labeled as <*e*> are in fact an imperfect estimate

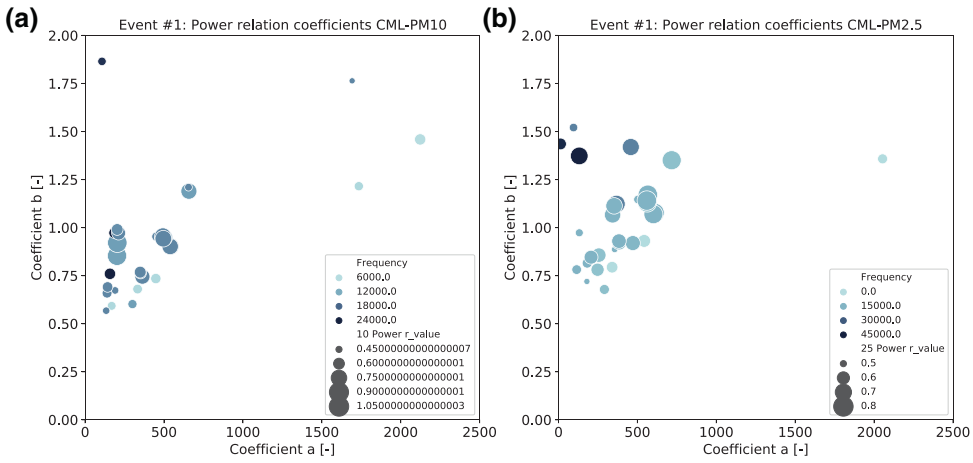

Figure 9. Coefficients *a* and *b* of the power relations between: (a) <*e*> and PM_{10} and (b) <*e*> and $PM_{2.5}$ for E#1.

of the RSL variance. Large observed fluctuations in link RSLs during haze events, ranging from typical values of 0.1 dB to up to 5 dB or more, led to observed <*e*> of up to 2 or 3 dB km^{-1}. These very large fluctuations were unlikely to be due to turbulence only, for example, scintillation phenomena due to fluctuations in C_n^2, which would produce variations in RSLs of orders of magnitude less (Marzano & d'Auria, 1998). Furthermore, conditions observed in the ABL during these events were typically characterized by low humidity, therefore having lower variations in C_Q^2 and consequently less susceptibility to scintillations at radio frequencies.

The predominant mechanism causing fluctuations in RSLs was most likely due to strong spatial contrasts in the air refraction index, such as ducting phenomena. Atmospheric soundings at Melbourne airport systematically showed the occurrence of surface-based ducts during each of the haze events in the evening soundings (9 p.m. AEDT; 12:00 UTC) the night preceding high concentrations of PM. For one of the events (E#3), surface-based ducting conditions were also observed in the morning soundings (9 a.m. AEDT; 00:00UTC), an indication that ducting conditions might have persisted during daytime on the 13th of January. This 2-day event (E#3) differed from the other events, with its surface-based duct having a higher base (at ~300 m AGL), resulting in smaller variations in RSL and <*e*>. In addition to increases in <*e*> during ducting events, the weather radar Z_{95} also showed significant increases of up to 6 dB, being were well above its baseline and not attributed to any other phenomenon. The S-Band radar is sensitive to ducting: its ground clutter within the 10 km radius (e.g., via the Z_{95}) would first see elevation rays (0.5°) trapped in the near-surface subrefractive surface layer and capped below a strong duct, or within the duct to produce higher values of ground clutter returns as compared to normal propagation conditions. The absence of an increase in the Z_{95} during the first night of E#3 can be explained by a higher base for the surface-based duct during that night, so that the first elevation ray was traveling in normal or slightly subrefractive conditions. Event #4 is peculiar in that the concentrations in $PM_{2.5}$ remained low as compared to other events, while large variations in <*e*> were observed. These could be linked to large values of PM_{10} as measured by in situ measurements, or anomalous propagation conditions could have been present, without high concentrations of $PM_{2.5}$ (a case of false positive). A climatology of anomalous propagation conditions and atmospheric stability in this region should be the focus of future research.

4.2. Reliability of Retrievals for $PM_{2.5}$ and PM_{10}

Power-law regressions between <*e*> and PM concentrations measured at nearby stations led to varying correlation coefficients and RMSE depending on the event, and the location of the links. Relatively high correlation coefficients and low RMSE were observed across the full domain for E#1, while high correlation coefficients and low RMSE were only observed in the south-eastern part of the domain for E#3. These disparities were related to the nature of the duct (its geometry, homogeneity, and spatial extend) and the relative geometry of the links. In the case of E#1, the surface-based duct as observed at Melbourne airport had a base around 100 m AGL or less, while in the case of E#3, the surface-based duct had a much higher base (around 300 m). This surface-based duct with higher base is expected to lead to slight subrefractivity conditions within the atmospheric layer where links operate, resulting in small variations in signal and values of <*e*>. Conversely, the surface-based duct of E#1 with a base height located just above or within the surface layer in which most links EM propagated, is expected to enable transmitted EM signals to be conducted within the duct or refracted back to the surface, creating multipaths, and therefore a large increase or decrease of RSLs and large values of <*e*>. In the case of E#3, the event lasted almost 2 days including a full period of daylight. Variations of the refractive index during daylight, and for a convective mixed layer could be drastically different than during night-time, with daytime convection deepening the mixing layer and reducing stratification. This can be seen in the potential temperature profile (Figure 6) on the 14th January at 00:00 UTC, with the base of the stratified layer being lifted at 400 AGL as compared to the morning sounding of the same day.

Because of the high particulate concentrations in the ABL, during daytime, solar radiation in the shortwave will be absorbed and slightly increase the temperature of the upper ABL, and reduce the shortwave radiation reaching the ground (Robock, 1988, 1991). This would contribute to maintaining stable conditions in the upper ABL and act as a lid, suppressing dispersion of PM through convection. However, in the case

of E#3, the convective boundary layer would have been maintained during daytime between 0 and above 400 m AGL (probably significantly higher as the 00:00 UTC would have seen subsidence after sunset) and created "normal" propagation or slightly subrefractive conditions of propagation within this layer and the atmospheric volume within which the links operated.

Values of the power relation coefficients a and b were analyzed for E#1 as the correlation coefficients and RMSE were favorable. The relatively small spread of coefficients across all links and frequencies (>100 links) indicated some stability in the retrievals. The link geometry (elevation of transmitter and receivers AGL and effective path height) was not taken into account and could be a factor of variability in the coefficients: each link sampled a specific volume of the near-surface atmosphere, including varying air parcel characteristics and concentrations. Thus, a direct comparison of an integrated volume with point ground-level PM concentrations would be subject to spatiotemporal discrepancies, similarly to a comparison between a rain-gauge, a radar product and radio links (de Vos et al., 2018b). Here, hourly data were analyzed, re-sampling 15 min data from radio links to hourly intervals, and the effect of temporal resolution of RSL simultaneously with PM concentration will need to be explored in further research. The CML network is evolving rapidly and the newest generation of mobile telecommunication (5G) relies mostly on shorter links (a few km or less) with higher frequencies (71–76 and 81–86 GHz) (Fencl et al., 2020). The effect of smoke on these new high frequency links remains unknown and future work should include data from the 5G infrastructure.

4.3. Mechanisms for Smoke Dispersion Within the ABL

Ultimately, the propagation of EM within the ABL is driven by fluctuations of air parcel properties, mechanical and convective turbulence, wind shear and potential stratification. This characterization of the ABL structure was essentially based on vertical atmospheric soundings at one location and twice a day, which did not encompass the complexity of smoke entrainment and dispersion within the ABL and in the free troposphere, and interactions with other air masses at meso and local scales. There was spatiotemporal variability in the formation and persistence of ducting propagation conditions observed via the variations in $<e>$ which peaked at different times and for different intensities and durations. This variability in observed $<e>$ together with the geometry of the links provides spatial information on the ABL structure. However, additional observations of the ABL structure would help to better understand the full-scale and interplay of processes during smoke haze events. The process of fumigation, which describes the entrainment of a fumigant parcel within a mixed layer such as the ABL, has been analyzed through laboratory-based experiments (Deardoff et al., 1982) and further described for a real-case study during a smoke haze event on the U.S. east coast (Pahlow et al., 2005). In that work, lidar observations were essential in identifying smoke dispersion within the ABL and its temporal evolution (Sapkota et al., 2005). Doppler lidar observations (Lareau & Clements, 2015) together with more frequent and spatially distributed atmospheric soundings would fill the gap in monitoring in order to comprehensively take into account all processes to monitor smoke concentrations within the ABL during these events.

5. Conclusion

This study analyzed RSLs from radio links, together with ground meteorological and atmospheric sounding observations and weather radar ground data, to examine PM concentration levels for a series of smoke haze events in Greater Melbourne, Australia. These smoke haze events were induced by smoke released from fire fronts located hundreds of km away and transported via various dispersion mechanisms to the surface layer of the ABL and at the ground level.

Vertical atmospheric soundings showed a systematic occurrence of elevated temperature inversions of varying depths within the ABL at night-time during these events; such an elevated inversion (between 400 and 800 m AGL) was also observed during daytime for one of the events, capping the mixed layer below. These inversions are hypothesized to be triggered by the combined mechanism of smoke subsidence and mixing through downdrafts from the free troposphere to the ABL, and further absorption of shortwave radiation that helped increase the potential temperature of these layers, while reducing radiation reaching ground level, lowering convection. This layering of warmer air above a thin layer of colder air systematically created surface-based ducts at elevations ranging from typically 100 m AGL, except for one event where the

surface-based duct base was located higher at 300 m AGL. The joint analysis of radio link data showed large variations in RSLs during these events, a pattern typically associated with anomalous propagation conditions. Available RSLs from radio links were sampled at 15 min intervals, and the difference between minima and maxima over that interval defined as the entropy $<e>$. The magnitude of fluctuations as seen in $<e>$ were hypothesized to be proportional to the PM concentration, with power-law relations between $PM_{2.5}$ and PM_{10} derived.

There remained uncertainty on the horizontal extent of the surface-based duct and its temporal evolution, as related to the smoke PM concentration. Previous studies analyzing smoke entrainment within the ABL have shown that Lidar can provide the fine temporal characterization of ABL processes, due to aerosols that can be used as effective tracers. This combined with frequent atmospheric soundings during day and night-time would make a full description of the ABL structure and temporal evolution possible. In this study, only the average, minimum and maximum of 15 min interval received signals were available, thus capturing only a portion of the variability of the signal, that is, the outer shape of the distribution of the RSL over that interval. The high temporal resolution of RSLs would allow finer analyses to be conducted and to derive the signal variance, which could be a better indicator than the entropy as defined herein. CMLs supporting the 5G network have substantially different characteristics, that is, higher frequencies and shorter pathlengths, as compared to the existing CMLs. The effect of smoke on the RSLs of these higher frequency links should be a new area of investigation. Gathering of larger amounts of data for similar events (such as the several week-long events that happened in Sydney and Canberra in 2019–2020) would enable the use of timeseries classification tools like Long-Short Term Memory deep learning algorithms, in order to analyze and retrieve desired proxies, including PM concentrations or atmospheric gases such as CO, NO_x, or O_3. A potential application of smoke PM concentration retrievals through CMLs is for regional agricultural fires that are often burning through smoldering combustion, in particular in the Asia-Pacific region where these are very common at certain periods of the year. The particles generated from these fires are of micron-size and would possibly induce similar anomalous propagation conditions at the land surface.

The best performing smoke retrievals showed relatively modest qualitative skills (correlation coefficients between 0.5 and 0.7 and RMSE close to 50 $\mu g\ m^{-3}$). Hence, the qualitative information deduced from CML data might, instead of providing a stand-alone retrieval of smoke particulate concentration, rather be used within a larger modeling framework including other data sources such as satellite imagery, social media data (Ford et al., 2017), and in situ observations of PM concentrations. Most importantly, CML signals enable the identification of anomalous propagation conditions, and in turn qualitative and spatially distributed information on atmospheric stability. Temperature inversion conditions can be the precursors of or are associated with elevated PM concentrations; there is a strong feedback between the two, positively enhancing both the strength of the stratification and the magnitude of smoke concentrations. One barrier to a more generalized used of CML data is the potentially wider availability of such privately owned data sets: there remains a large variability in the conditions of access to such data. In the present case data was accessible to the authors but protected by a Non-Disclosure agreement, as seen also in Graf et al. (2020), while in others the data is freely available (de Vos et al., 2018a) or available upon purchase (Roversi et al., 2020). The uniqueness of CML data is their worldwide distribution, and the presence of infrastructure collecting data in remote and unmonitored regions where other techniques are unavailable. One of the drawbacks in the retrievals is the associated inaccuracies caused by the presence of other atmospheric phenomena such as rainfall or fog: future research should be conducted on these potentially simultaneous physical impacts on signal levels.

Conflict of Interest

The authors declare no conflicts of interest relevant to this study.

Data Availability Statement

Radio links data are not publicly available due to a Non-Disclosure Agreement. Air quality data, automatic weather station data, and weather radar have been made available at: https://doi.org/10.5281/zenodo.3965058

Acknowledgments
Australian Research Council Discovery Project Grant number DP160101377 funded this project. Thanks to Dr Vincent Villani from the Australian Bureau of Meteorology for sourcing the Himawari-8 images presented herein. Thanks to the Environmental Protection Authority Victoria for providing the air quality data presented in this study. We acknowledge the traditional Owners and Elders past and present of all the lands where this research was conducted. Thanks to the Editor and the two reviewers for their comments that contributed to improve the quality of the manuscript.

References

Ahmadov, R., Grell, G., James, E., Csiszar, I., Tsidulko, M., Pierce, B., et al. (2017). Using VIIRS fire radiative power data to simulate biomass burning emissions, plume rise and smoke transport in a real-time air quality modeling system. *In 2017 IEEE International Geoscience and Remote Sensing Symposium* (IGARSS) (pp. 2806–2808). Fort Worth, TX: IEEE. https://doi.org/10.1109/IGARSS.2017.8127581

Andreas, E. L. (1989). Two-wavelength method of measuring path-averaged turbulent surface heat fluxes. *Journal of Atmospheric and Oceanic Technology*, *6*, 280–292. https://doi.org/10.1175/15200426(1989)006<0280:TWMOMP>2.0.CO;2

Arvola, W. A. (1957). Refractive index profiles and associated synoptic patterns. *Bulletin of the American Meteorological Society*, *38*(4), 212–220. https://doi.org/10.1175/1520-0477-38.4.212

Boer, M. M., de Dios, V. R., & Bradstock, R. A. (2020). Unprecedented burn area of Australian mega forest fires. *Nature Climate Change*, *10*(3), 171–172. https://doi.org/10.1038/s41558-020-0716-1

Borchers Arriagada, N., Palmer, A. J., Bowman, D. M., Morgan, G. G., Jalaludin, B. B., & Johnston, F. H. (2020). Unprecedented smoke-related health burden associated with the 2019–20 bushfires in eastern Australia. *The Medical Journal of Australia*, *213*, 282–283. https://doi.org/10.5694/mja2.50545

Chou, Y.-H., & Kiang, J.-F. (2014). Ducting and turbulence effects on radio-wave propagation in an atmospheric boundary layer. *Progress In Electromagnetics Research B*, *60*, 301–315. https://doi.org/10.2528/pierb14062201

Chung, A., Chang, D. P., Kleeman, M. J., Perry, K. D., Cahill, T. A., Dutcher, D., et al. (2001). Comparison of real-time instruments used to monitor airborne particulate matter. *Journal of the Air & Waste Management Association*, *51*(1), 109–120. https://doi.org/10.1080/10473289.2001.10464254

David, N., Alpert, P., & Messer, H. (2009). Technical Note: Novel method for water vapour monitoring using wireless communication networks measurements. *Atmospheric Chemistry and Physics*, *9*, 2413–2418. https://doi.org/10.5194/acp-9-2413-2009

David, N., Alpert, P., & Messer, H. (2013). The potential of commercial microwave networks to monitor dense fog-feasibility study. *Journal of Geophysical Research: Atmospheres*, *118*, 11750–11761. https://doi.org/10.1002/2013JD020346

David, N., & Gao, H. O. (2016). Using Cellular Communication Networks To Detect Air Pollution. *Environmental Science & Technology*, *50*(17), 9442–9451. https://doi.org/10.1021/acs.est.6b00681

Deardorff, J. W., & Willis, G. E. (1982). Ground-level concentrations due to fumigation into an entraining mixed layer. *Atmospheric Environment*, *16*(5), 1159–1170. https://doi.org/10.1016/0004-6981(82)90205-0

Deardoff, J. W., Willis, G. E., & Lilly, D. K. (1969). Laboratory Investigation of Nonsteady Penetrative Convection. *Journal of Fluid Mech.*, *35*, 7–31.

De Bruin, H. (2002). Introduction: Renaissance of scintillometry. *Boundary-Layer Meteorology*, *105*, 1–4. https://doi.org/10.1023/A:1019628124829

de Vos, L. W., Overeem, A., Leijnse, H., & Uijlenhoet, R. (2018a). Rainfall estimation accuracy of a nationwide instantaneously sampling commercial microwave link network: Error dependency on known characteristics. *Journal of Atmospheric and Oceanic Technology*, *36*(10), 1267–1283. https://doi.org/10.1175/JTECH-D-18-0197.1

de Vos, L. W., Raupach, T. H., Leijnse, H., Overeem, A., Berne, A., & Uijlenhoet, R. (2018b). High-resolution simulation study exploring the potential of radars, crowdsourced personal weather stations, and commercial microwave links to monitor small-scale urban rainfall. *Water Resources Research*, *54*, 10293–10312. https://doi.org/10.1029/2018WR023393

Dowdy, A. J., & Pepler, A. (2018). Pyroconvection risk in Australia: Climatological changes in atmospheric stability and surface fire weather conditions. *Geophysical Research Letters*, *45*(4), 2005–2013. https://doi.org/10.1002/2017GL076654

Fabry, F. (2015). *Radar meteorology: Principles and practice*. Cambridge University Press.

Fencl, M., Dohnal, M., Valtr, P., Grabner, M., & Bares, V. (2020). Atmospheric observations with E-band microwave links – Challenges and opportunities. *Atmospheric Measurement Techniques*, *13*, 6559–6578. https://doi.org/10.5194/amt-13-6559-2020

Ford, B., Burke, M., Lassman, W., Pfister, G. & Pierce, J. R. (2017). Status update: Is smoke on your mind? Using social media to assess smoke exposure. *Atmospheric Chemistry and Physics*, *17*, 7541–7554. https://doi.org/10.5194/acp-17-7541-2017

Frehlich, R. (2000). Simulation of laser propagation in a turbulent atmosphere. *Applied Optics*, *39*, 393–397. https://doi.org/10.1364/AO.39.000393

Goodrick, S. L., Achtemeier, G. L., Larkin, N. K., Liu, Y., & Strand, T. M. (2013). Modelling smoke transport from wildland fires: A review. *International Journal of Wildland Fire*, *22*(1), 83–94. https://doi.org/10.1071/WF11116

Graf, M., Chwala, C., Polz, J., & Kunstmann, H. (2020). Rainfall estimation from a German-wide commercial microwave link network: Optimized processing and validation for 1 year of data. *Hydrology and Earth System Sciences*, *24*, 2931–2950. https://doi.org/10.5194/hess-24-2931-2020

Gupta, P., Christopher, S. A., Box, M. A., & Box, G. P. (2007). Multi-year satellite remote sensing of particulate matter air quality over Sydney, Australia. *International Journal of Remote Sensing*, *28*(20), 4483–4498. https://doi.org/10.1080/01431160701241738

Hill, R. J., Clifford, S. F., & Lawrence, R. S. (1980). Refractive-index and absorption fluctuations in the infrared caused by temperature, humidity, and pressure fluctuations. *Journal of the Optical Society of America*, *70*(10), 1192. https://dx.doi.org/10.1364/josa.70.001192

ITU-R P.453-14 (2019). *The radio refractive index: Its formula and refractivity data*. Retrieved from https://www.itu.int/dms_pubrec/itu-r/rec/p/R-REC-P.453-14-201908-I!!PDF-E.pdflast

Jones, M. W., Smith, A., Betts, R., Canadell, J. G., Prentice, I. C., & Le Quere, C. (2020). *Climate change increases the risk of wildfires*. University of East Anglia. Retrieved from https://sciencebrief.org/briefs/wildfires

Kablick, G. P., Allen, D. R., Fromm, M. D., & Nedoluha, G. E. (2020). Australian pyroCb smoke generates synoptic-scale stratospheric anticyclones. *Geophysical Research Letters*, *47*, e2020GL088101. https://doi.org/10.1029/2020GL088101

Keywood, M., Cope, M., Meyer, C. P., Iinuma, Y., & Emmerson, K. (2015). When smoke comes to town: The impact of biomass burning smoke on air quality. *Atmospheric Environment. 121*, 13–21. https://doi.org/10.1016/J.ATMOSENV.2015.03.050

Kim, H. C., Chai, T., Stein, A., & Kondragunta, S. (2020). Inverse modeling of fire emissions constrained by smoke plume transport using HYSPLIT dispersion model and geostationary satellite observations. *Atmospheric Chemistry and Physics*, *20*, 10259–10277. https://doi.org/10.5194/acp-20-10259-2020

Kochanski, A. K., Mallia, D. V., Fearon, M. G., Mandel, J., Souri, A. H., & Brown, T. (2019). Modeling wildfire smoke feedback mechanisms using a coupled fire-atmosphere model with a radiatively active aerosol scheme. *Journal of Geophysical Research: Atmospheres*, *124*(16), 9099–9116. https://doi.org/10.1029/2019JD030558

Kohsiek, W., & Herben, M. H. A. J. (1983). Evaporation derived from optical and radio-wave scintillation. *Applied Optics*, *22*(17), 2566–2570. https://doi.org/10.1364/AO.22.002566

Lareau, N. P., & Clements, C. B. (2015). Cold smoke: Smoke-induced density currents cause unexpected smoke transport near large wildfires. *Atmospheric Chemistry and Physics*, *15*, 11513–11520. https://doi.org/10.5194/acp-15-11513-2015

Larkin, N. K., O'Neill, S. M., Solomon, R., Raffuse, S., Strand, T., Sullivan, D. C., et al. (2010). The BlueSky smoke modeling framework. *International Journal of Wildland Fire*, *18*(8), 906–920. https://doi.org/10.1071/WF07086

Leijnse, H., Uijlenhoet, R., & Stricker, J. N. M. (2007). Rainfall measurement using radio links from cellular communication networks. *Water Resources Research*, *43*, W03201. https://doi.org/10.1029/2006WR005631

Liu, L. & Mishchenko, M. I. (2020). Spectrally dependent linear depolarization and lidar ratios for nonspherical smoke aerosols. *Journal of Quantitative Spectroscopy and Radiative Transfer*, *248*, 106953. https://doi.org/10.1016/j.jqsrt.2020.106953

Liu, Y., Kochanski, A., Baker, K. R., Mell, W., Linn, R., Paugam, R., et al. (2019). Fire behaviour and smoke modelling: Model improvement and measurement needs for next-generation smoke research and forecasting systems. *International Journal of Wildland Fire*, *28*(8), 570–588. https://doi.org/10.1071/WF18204

Louf, V., Protat, A., Warren, R. A., Collis, S. M., Wolff, D. B., Raunyiar, S., et al. (2019). An integrated approach to weather radar calibration and monitoring using ground clutter and satellite comparisons. *Journal of Atmospheric and Oceanic Technology*, *36*, 17–39. https://doi.org/10.1175/JTECH-D-18-0007.1

Marzano, F. S. & d'Auria, G. (1998). Model-based prediction of amplitude scintillation variance due to clear-air tropospheric turbulence on Earth-satellite microwave links. *IEEE Transactions on Antennas and Propagation*, *46*(10), 1506–1518. https://doi.org/10.1109/8.725283

McCarthy, N., Guyot, A., Dowdy, A., & McGowan, H. (2018). Wildfire and weather radar: A review. *Journal of Geophysical Research: Atmospheres*, *124*, 266–286. https://doi.org/10.1029/2018JD029285

McCarthy, N., Guyot, A., Protat, A., Dowdy, A. J., & McGowan, H. (2020). Tracking pyrometeors with meteorological radar using unsupervised machine learning. *Geophysical Research Letters*, *47*, 84305. https://doi.org/10.1029/2019GL084305

Mentes, Ş., & Kaymaz, Z. (2007). Investigation of surface duct conditions over Istanbul, Turkey. *Journal of Applied Meteorology and Climatology*, *46*, 318–337. https://doi.org/10.1175/JAM2452.1

Messer, H., Zinevich, A., & Alpert, P. (2006). Environmental monitoring by wireless communication networks. *Science*, *312*(5774), 713. https://doi.org/10.1126/science.1120034

Pahlow, M., Kleissl, J., & Parlange, M. B. (2005). Atmospheric boundary-layer structure observed during a haze event due to forest-fire smoke. *Boundary-Layer Meteorology*, *114*(1), 53–70. https://doi.org/10.1007/s10546-004-6350-z

Pudashine, J., Guyot, A., Petitjean, F., Pauwels, V. R. N., Uijlenhoet, R., Seed, A., & Walker, J. P. (2020). Deep learning for an improved prediction of rainfall retrievals from commercial microwave links. *Water Resources Research*, *55*, e2019WR026255. https://doi.org/10.1029/2019WR026255

Rao, T. R., Rao, V. B., Prasad, M., Sarkar, S. K., & Lakshmi, D. R. (1999). Effect of sea breeze on propagation characteristics over a LOS microwave link located in Indian south-east ocean. *Indian Journal of Radio and Space Physics*, *28*, 113–118.

Reisen, F., Duran, S. M., Flannigan, M., Elliott, C., & Rideout, K. (2015). Wildfire smoke and public health risk. *International Journal of Wildland Fire*, *24*(8), 1029–1044. https://doi.org/10.1071/WF15034

Reisinger, A., Kitching, R. L., Chiew, F., Hughes, L., Newton, P. C. D., Schuster, S. S., et al. (2014). Australasia. In V. R. Barros, C. B. Field, D. J. Dokken, M. D. Mastrandrea, K. J. Mach, T. E. Bilir, et al. (Eds.), *Climate Change 2014: Impacts, adaptation, and vulnerability. Part B: Regional aspects. Contribution of Working Group II to the Fifth Assessment Report of the Intergovernmental Panel on Climate Change* (pp. 1371–1438). Cambridge, UK and New York, NY: Cambridge University Press.

Robock, A. (1988). Enhancement of surface cooling due to forest fire smoke. *Science*, *242*, 911–913. Retrieved from https://www.jstor.org/stable/1701971

Robock, A. (1991). Surface cooling due to forest fire smoke. *Journal of Geophysical Research*, *96*(D11), 20869–20878. https://doi.org/10.1029/91JD02043

Roversi, G., Alberoni, P. P., Fornasiero, A., & Porcù, F. (2020). Commercial microwave links as a tool for operational rainfall monitoring in Northern Italy. *Atmospheric Measurement Techniques*, *13*, 5779–5797. https://doi.org/10.5194/amt-13-5779-2020

Sapkota, A., Symons, J. M., Kleissl, J., Wang, L., Parlange, M. B., Ondov, J., et al. (2005). Impact of the 2002 Canadian forest fires on particulate matter air quality in Baltimore City. *Environmental Science & Technology*, *39*(1), 24–32. https://doi.org/10.1021/es035311z

Shukla, P. R., Skea, J., Calvo Buendia, E., Masson-Delmotte, V., Pörtner, H.-O., Roberts, D. C., et al. (2019). *Climate change and land: An IPCC special report on climate change, desertification, land degradation, sustainable land management, food security, and greenhouse gas fluxes in terrestrial ecosystems*. Geneva, Switzerland: IPCC.

Tatarskii, V. I. (1961). In A. Silverman (Ed.), *Wave Propagation in a Turbulent Medium*. New York: McGraw-Hill.

Tatarskii, V. I. (1971). The Effects of the Turbulent Atmosphere on Wave Propagation. Springfield, VA: National Technical Information Service.

Tian, J., & Chen, D. (2010). A semi-empirical model for predicting hourly ground-level fine particulate matter (PM2.5) concentration in southern Ontario from satellite remote sensing and ground-based meteorological measurements. *Remote Sensing of Environment*, *114*(2), 221–229. https://doi.org/10.1016/j.rse.2009.09.011

Tunick, A. (2003). CN2 model to calculate the micrometeorological influences on the refractive index structure parameter. *Environmental Modelling & Software*, *18*(2), 165–171. https://doi.org/10.1016/S1364-8152(02)00052-X

Wu, Y., Arapi, A., Huang, J., Gross, B. & Moshary, F. (2018). Intra-continental wildfire smoke transport and impact on local air quality observed by ground-based and satellite remote sensing in New York City. *Atmospheric Environment*, *187*, 266–281. https://doi.org/10.1016/j.atmosenv.2018.06.006

Xing, Y. F., Xu, Y. H., Shi, M. H., & Lian, Y. X. (2016). The impact of PM2.5 on the human respiratory system. *Journal of Thoracic Disease*, *8*(1), E69–E74. https://doi.org/10.3978/j.issn.2072-1439.2016.01.19